



Ultrafast many-body bright-dark exciton transition in anatase TiO₂

Aolei Wang^a, Xiang Jiang^{b,1}, Qijing Zheng^a, Hrvoje Petek^c, and Jin Zhao^{a,b,c,d,1}

Edited by Catherine Murphy, University of Illinois at Urbana-Champaign, Urbana, IL; received May 7, 2023; accepted September 29, 2023

The momentum-forbidden dark excitons can have a pivotal role in quantum information processing, Bose-Einstein condensation, and light-energy harvesting. Anatase TiO₂ with an indirect band gap is a prototypical platform to study bright to momentum-forbidden dark exciton transition. Here, we examine, by GW plus the real-time Bethe-Salpeter equation combined with the nonadiabatic molecular dynamics (GW + rtBSE-NAMD), the many-body transition that occurs within 100 fs from the optically excited bright to the strongly bound momentum-forbidden dark excitons in anatase TiO₂. Comparing with the single-particle picture in which the exciton transition is considered to occur through electron-phonon scattering, within the GW + rtBSE-NAMD framework, the many-body electron-hole Coulomb interaction activates additional exciton relaxation channels to notably accelerate the exciton transition in competition with other radiative and nonradiative processes. The existence of dark excitons and ultrafast bright-dark exciton transitions sheds insights into applications of anatase TiO₂ in optoelectronic devices and light-energy harvesting as well as the formation process of dark excitons in semiconductors.

bright-dark exciton transition | anatase TiO₂ | GW + real-time BSE | many-body effects

Excitons are correlated electron–hole (e-h) pairs that are bound as hydrogenic quasiparticles (QPs) through the screened Coulomb attraction. They are engaged as carriers of energy, spin, and information q-bits in various light-harvesting and optoelectronic materials, including organic (1–3), metal-halide perovskites (4–6), transition metal dichalcogenides (7-9), metal oxides (10-13), single and compound semiconductors (14, 15), etc. Compared with the optically accessible bright excitons, the momentum-forbidden dark excitons usually have longer lifetimes because electrons and holes are separated in momentum space, and their recombination requires the second-order assistance by phonons (8, 16–18). Research interest in dark excitons has rapidly grown because their extended lifetimes make them attractive in potential applications such as quantum information processing, Bose-Einstein condensation, and light harvesting (8, 19-25). For these reasons, understanding how the bright-dark exciton transitions on ultrafast time scales depend on the material structure and composition is of broad interest (18, 25–27).

Anatase TiO₂ is one of the most studied metal-oxide semiconductors with important applications in photocatalysis, photovoltaics, and sensors (28-39). Previous studies have reported that the direct optical band gap of anatase TiO₂ is dominated by a strongly bound exciton with intermediate Wannier-Mott and Frenkel character, which has a peculiar two-dimensional (2D) wavefunction within its three-dimensional (3D) lattice that exhibits remarkable exciton-phonon interactions (12, 40). The fundamental band gap of anatase is indirect (41, 42), such that the bright exciton forms by direct optical *e-h* pair excitation at around 0.4 eV higher energy. The bright exciton must release this excess energy by relaxing through energy and momentum scattering to the band edge. Such relaxation pathways of bright excitons are inextricably linked to applications in photonic and light-harvesting devices. Nevertheless, whether electrons and holes at the band edges are uncorrelated, or whether they form correlated e-h pairs of momentum-forbidden dark excitons, is still not established. One may expect that a bright-dark exciton transition is led by electron-phonon (e-ph) scattering, but many-body e-h interactions may also contribute to its formation. To unravel dark exciton formation dynamics, a real-time ab initio investigation explicitly including many-body interactions is essential.

The benchmark state-of-the-art ab initio theory approach to describe exciton quasiparticle properties in a condensed phase is the GW plus Bethe–Salpeter equation (GW + BSE) method (43-45). The GW calculation obtains the QP energy levels based on the many-body perturbation theory, while BSE describes the screened *e-h* pair Coulomb interaction. The GW + BSE method is widely used to calculate the "static" electronic structures and their interactions in forming excitons in a broad range of materials (42, 46-49). While providing realistic band structure descriptions, it has a prohibitive demand on the computational resources. The implementation of GW + BSE for exciton dynamics has awaited efficient

Significance

The dark excitons are proposed to play an important role in different fields including quantum information processing and Bose-Einstein condensation. Anatase TiO₂, which exhibits both a bright exciton and an indirect band gap, it is expected to provide prototypical platform to understand the transition from bright to momentum-forbidden dark exciton. In this work, using GW + real-time propagation of BSE, we reveal that with respect to the conventional electronphonon mechanism, the manybody electron-hole Coulomb interaction activates additional exciton relaxation channels that notably accelerate the brightdark transition. It sheds insights into the formation of dark exciton in semiconductors.

Author affiliations: aDepartment of Physics, University of Science and Technology of China, Hefei 230026, China; bInternational Center for Quantum Design of Functional Materials/Hefei National Research Center for Physical Sciences at the Microscale, University of Science and Technology of China, Hefei 230026, China; 'Department of Physics and Astronomy and the IQ Initiative, University of Pittsburgh, Pittsburgh, PA 15260; and dHefei National Laboratory, University of Science and Technology of China, Hefei 230088, China

Author contributions: H.P. and J.Z. designed research; A.W. performed research; A.W., X.J., and Q.Z. contributed new reagents/analytic tools; A.W. and J.Z. analyzed data; and A.W., Q.Z., H.P., and J.Z. wrote the paper.

The authors declare no competing interest.

This article is a PNAS Direct Submission.

Copyright © 2023 the Author(s). Published by PNAS. This article is distributed under Creative Commons Attribution-NonCommercial-NoDerivatives License 4.0

¹To whom correspondence may be addressed. Email: jxiang@mail.ustc.edu.cn or zhaojin@ustc.edu.cn.

This article contains supporting information online at https://www.pnas.org/lookup/suppl/doi:10.1073/pnas. 2307671120/-/DCSupplemental.

Published November 13, 2023.

algorithms to be developed (50). We apply such GW + real-time propagation of the BSE approach combined with the nonadiabatic molecular dynamics (GW + rtBSE-NAMD) to perform a study at the ab initio theory level of real-time exciton relaxation dynamics interacting with a phonon bath (50).

Using this approach, we examine the ultrafast bright-dark exciton transition stimulated by many-body effects in anatase TiO2. First, using GW + BSE, we find a strongly bound momentum-forbidden dark exciton to be formed by the interaction of an electron at Γ and a hole at X points (hereafter, the Γ -X exciton). The calculated e-hpairs' binding energy of the bright exciton formed by excitation along the Γ -Z direction is 216 meV, while that of the dark Γ -X exciton is comparably strong 197 meV at zero temperature. Performing single-particle nonadiabatic molecular dynamics (NAMD) calculation gives a bright- Γ - Γ to dark- Γ -X exciton transition in 300 fs by e-ph scattering mediated hole transfer from Γ to X. By contrast, applying the many-body GW + rtBSE-NAMD approach, we reveal that the e-h Coulomb interaction activates additional exciton relaxation channels that accelerate the bright-dark transition to less than 100 fs. This demonstrates that the many-body Coulomb interaction can dramatically enhance the bright-dark exciton transition with respect to the conventional e-ph scattering and is the dominant relaxation mechanism in high-energy photochemical and photophysical processes in anatase. The existence of strongly bound dark exciton and many-body correlations leading to its formation in anatase TiO₂ provides insights into its potential applications in light-energy harvesting and quantum-information processing.

Results

Existence of the Momentum-Forbidden Dark Exciton. Before we investigate the properties of the momentum-forbidden dark exciton, it is instructive to establish the properties of the bright direct exciton in anatase TiO_2 . Fig. 1*A* shows the calculated band structure of anatase TiO_2 , where the dotted and red solid lines represent the PBE and G_0W_0 results, respectively (see more details in *Materials and Methods* and *SI Appendix*). The G_0W_0 calculation

gives an indirect band gap of 3.60 eV and a direct band gap of 3.92 eV. Compared to the PBE band structure, the correction of G_0W_0 can be understood as a rigid shift of bands.

Fig. 1B shows the anatase optical spectra in the uncorrelated e-h picture obtained with G₀W₀-RPA (mauve line) and the exciton picture by solving the BSE equation on top of the G₀W₀ (blue line). The exciton optical spectrum is calculated by solving the BSE using the Hefei-NAMD code (52). The G₀W₀-RPA peak locates at 3.92 eV, corresponding to the direct QP band gap, while the G_0W_0 -BSE spectrum is structured with peak at 3.69 eV, which corresponds to bright direct exciton absorption in anatase TiO₂. The bright exciton has contributions from the direct e-h pair excitation for k-points along the Γ -Z direction, that are indicated by the orange arrows in Fig. 1A. Relating the direct QP band gap (3.92 eV) in the G_0W_0 -RPA spectra to the direct bright exciton peak in the G_0W_0 -BSE optical spectra (3.69 eV), gives the exciton binding energy of 223 meV, without considering any offset by the zero point energy renormalization (12, 53). Both the G_0W_0 and BSE results in Fig. 1 are in agreement with the previous investigation of the bright exciton (12), shown in Table 1.

As seen from the band structure in Fig. 1*A*, anatase TiO_2 has an indirect band gap where the conduction band minimum (CBM) is located at Γ and the valence band maximum (VBM) is near the X point. The G_0W_0+BSE calculation using the primitive cell cannot describe the momentum-forbidden indirect *e-h* pair. If we extend the primitive cell to a $2 \times 2 \times 1$ tetragonal supercell, however, the X point is folded into the Γ point of the supercell (as shown in Fig. 2 *A* and *B*), enabling the G_0W_0+BSE method to be applied to investigate the indirect $\Gamma-X$ *e-h* pair.

To proceed, using the inverse dielectric function obtained by the G_0W_0 calculation with primitive cell in VASP, we use the Hefei-NAMD code to perform the BSE calculation of the 2 × 2 × 1 supercell with 4 × 4 × 4 k-points (see more details in *Materials and Methods* and *SI Appendix*). In the lower panel of Fig. 2*C*, we plot the optical absorption spectra and analyze the contribution from different *e-h* pairs according to Eq. 5 in the *Materials and Methods*. Because the optical transition oscillator strengths for the

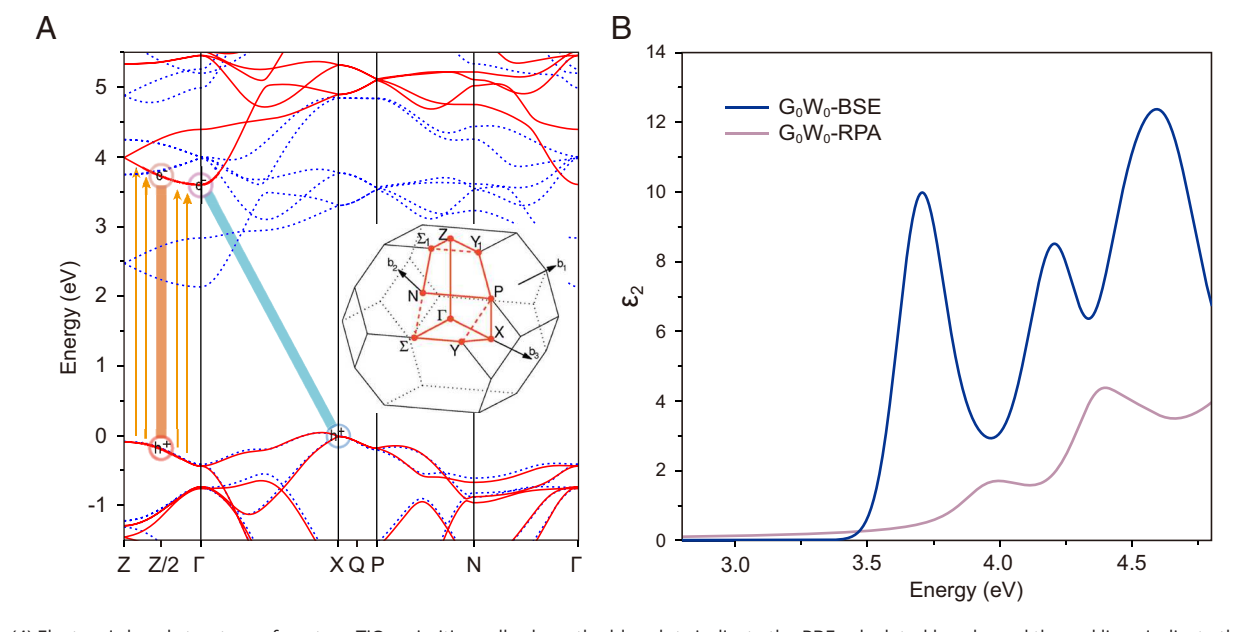


Fig. 1. (*A*) Electronic band structure of anatase TiO_2 primitive cell, where the blue dots indicate the PBE calculated bands, and the red lines indicate the values obtained after G_0W_0 corrections. The energy reference is the valence band maximum (VBM). The inset is the Brillouin zone of the anatase primitive cell (51). (*B*) Calculated optical spectra of pristine anatase TiO_2 . The imaginary part of the dielectric function, or the absorption spectrum, with the electric field polarized along the [100] direction.

Table 1. The QP band gaps, and direct bright and indirect dark exciton energies, binding energies, and radii in anatase TiO₂

		Direct			Indirect
	<i>T</i> (K)	1 × 1 × 1	2 × 2 × 1	ref. 12	2 × 2 × 1
QP band gap (eV)	0	3.92	3.92	3.96	3.60
	100		3.94		3.57
	300		3.99		3.55
Exciton energy (eV)	0	3.69	3.70	3.76	3.40
	100		3.75		3.38
	300		3.80		3.36
Exciton binding	0	223	216	200	197
	100		197		191
energy (meV)	300		194		198
Exciton radius (nm)	0	// (001) (e))	2.4	2.2
		// (001) (h)	2.4	2.5
		\perp (001) (e))	1.3	1.5
		⊥ (001) (h)	1.6	1.9

The data are obtained for different unit cells and temperatures. The results reported in ref. 12 are also listed.

indirect e-h pairs are very small, their signal will be silent in the optical spectra. Therefore, instead of the optical spectra, we plot the joint density of states (JDOS) of the indirect e-h pairs in the upper panel in Fig. 2C. Thus, the direct e-h pair signal can be seen

from the optical absorption spectra and the JDOS includes the contribution from both the direct and indirect *e-h* pair. One can see that there is a peak in the absorption spectra contributed by different direct *e-h* pairs along Γ -Z in the range of 3.6 to 3.9 eV, corresponding to the bright direct exciton. The largest contribution to its density is from the Z/2-Z/2 e-h pair, with 3.70 eV energy. Significantly, there is a lower energy peak in JDOS contributed by the Γ -X *e-h* pair at 3.40 eV. Its energy is 197 meV lower than the indirect QP band gap obtained by G₀W₀, indicating the existence of a strongly bound momentum-forbidden dark exciton. The binding energy of the dark exciton is smaller than that of the bright exciton by 19 meV at 0 K. The QP band gaps, exciton energies, and exciton binding energies of the bright and dark excitons are summarized in Table 1. We notice that the experimental measurements reported 3.2 eV as an indirect absorption gap (54, 55), which is smaller than the theoretical value. The deviation may be due to the influence of defects, doping, and polaron formation (42). There is also a possibility that G_0W_0 calculation overestimates the QP band gap (56-59). The QP and optical band gap, however, mainly affect the diagonal elements of the BSE Hamiltonian (see more details in Materials and *Methods*). The off-diagonal elements, which determine the exciton dynamics, are barely affected by the possible small overestimation of the band gap.

To further understand the strongly bound dark exciton, the excitonic squared modulus of electron and hole wavefunctions are plotted in Fig. 2D. The electron and hole wavefunctions for the bright exciton are also plotted for a contrast. It can be seen that

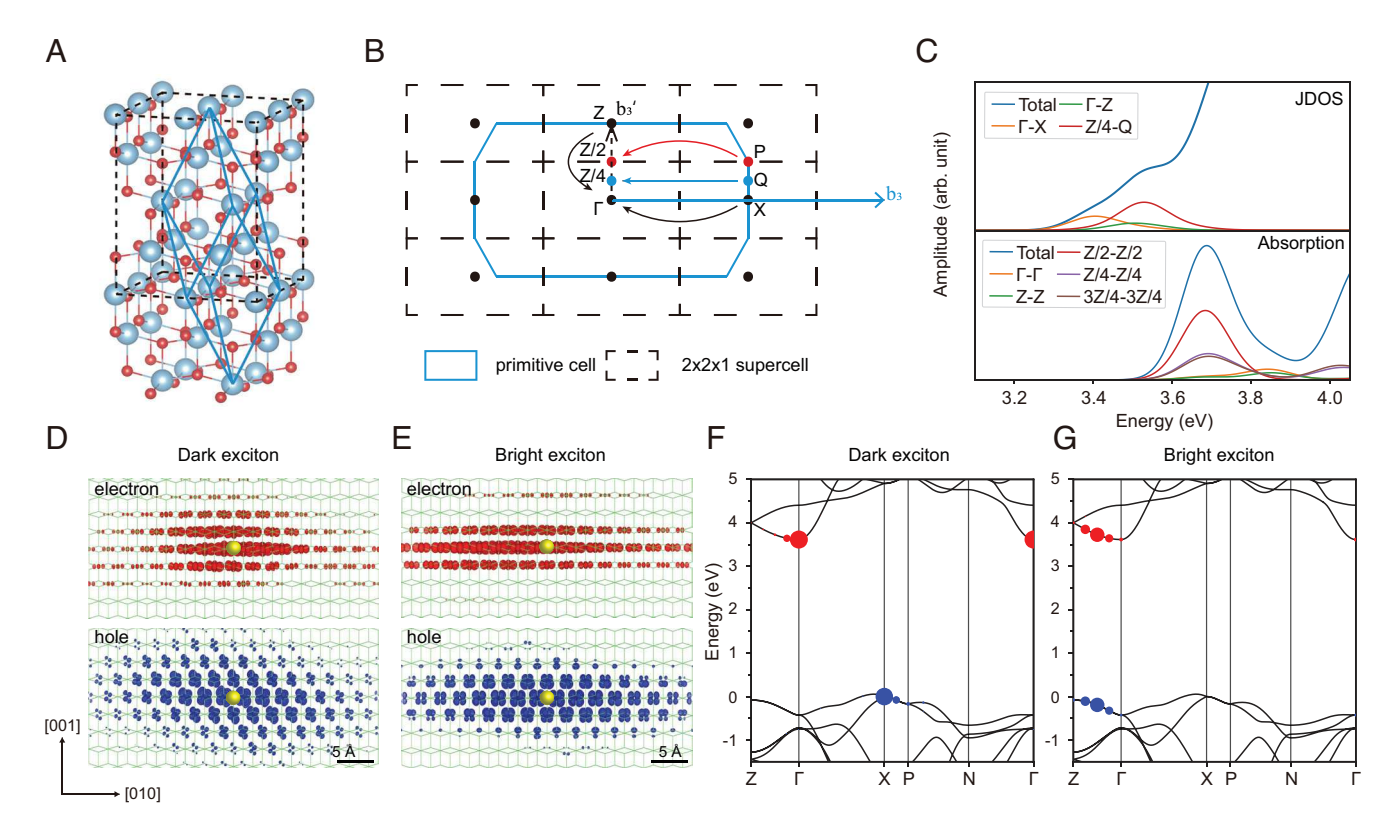


Fig. 2. (*A* and *B*) Atomic structure (*A*) and Brillouin zone (*B*) of anatase TiO_2 . The blue and red balls in (*A*) represent Ti and O atoms, respectively. The blue solid and black dashed lines in (*B*) describe the primitive cell and the $2 \times 2 \times 1$ supercell, respectively. The arrows indicate how the different k-points in the primitive cell Brillouin zone are folded into the supercell Brillouin zone. (*C*) Absorption spectrum contributed by different direct *e-h* pairs and the JDOS of indirect *e-h* pairs of the anatase $TiO_2 2 \times 2 \times 1$ supercell. (*D*–*G*) The distribution of wave functions of indirect dark exciton (*D* and *F*) and direct bright exciton (*E* and *G*) in real (*D* and *E*) and momentum (*F* and *G*) spaces. The upper (lower) panel in (*D* and *E*) corresponds to electron (hole) wavefunctions when the hole (electron) (represented by the yellow balls) of the considered excitonic pair is localized close to one oxygen (titanium) atom. The red and blue dots in (*F* and *G*) represent the electrons and holes, respectively. The size of the dots corresponds to the magnitude of the *e-h* pair distribution.

in the real space, whether it is a bright exciton or a dark exciton, the wave functions of their electron and hole are diffuse parallel to the (001) atomic plane. The difference appears in the direction perpendicular to the (001) plane, where the wavefunction of the bright exciton is relatively localized, exhibiting quasi-2D characteristics, while the dark exciton is more diffuse. The localized distribution in the real space corresponds to a diffuse distribution in the momentum space. Therefore, in Fig. 2 F and G, we can see that the bright exciton is contributed by multiple *e-h* pairs in the Γ-Z direction [perpendicular to the (001) plane], exhibiting a relatively diffuse characteristic in the momentum space. On the other hand, the dark exciton is contributed by electron at the Γ point and hole near the X point, showing a relatively localized behavior in the momentum space. Using a hydrogenic model, we have fit the radii of the electron and hole wavefunctions parallel and perpendicular to the (001) atomic plane. The results are shown in Table 1. From the binding energy and spatial nature, we conclude that the dark exciton has an intermediate character between the Frenkel and Wannier-Mott regimes.

Exciton-Phonon Interaction. In the GW + rtBSE-NAMD approach, phonon excitation is simulated using AIMD within periodic boundary conditions, and only phonons at the Γ point of the supercell Brillouin zone are included. Therefore, the sampling of phonon momentum depends on the size and shape of the supercell. For this purpose, we use a $2 \times 2 \times 1$ supercell to perform the AIMD simulation. Based on the rigid dielectric function approximation (see more details in *Materials and Methods*), the exciton energies along the AIMD trajectory can be obtained; the exciton energy fluctuation provides a measure of the exciton—phonon coupling.

We analyze phonon frequency dependence of the exciton-phonon coupling strength by representing Fourier transform (FT) spectra of the fluctuation amplitude. In Fig. 3, we plot the time-dependent QP and exciton energies along an AIMD trajectory of the supercell at 300 K and their FT spectra. The band unfolding technique is used to assign the corresponding band and k-point index in the primitive cell of all the states of the supercell. The VB is twofold degenerate along the Γ -Z and X-P line. In addition, the X, P, and Z/2 have two equivalent k-points when they are folded to the Brillouin supercell (BZ) of the supercell. Therefore, in the supercell, the points Γ and Zare two-fold degenerate, while the points X, P, and Z/2 are fourfold degenerate. During the AIMD simulation, the degeneracy is lifted, resulting in two energy levels at points Γ and Z, and four energy levels at points X, P, and $\mathbb{Z}/2$. The energy fluctuation amplitudes of VB@ Γ , CB@Γ, VB@Z/2, CB@Z/2, and VB@X QP energies range within 0.1 to 0.25 eV, while for the dark and bright excitons, they fluctuate by approximately 0.4 eV. This implies when an electron and a hole form an exciton, its coupling with phonons is enhanced compared with the uncorrelated electron and hole. For both the bright and dark excitons, there are three major peaks in the FT spectra, which are located at approximately 70, 330, and 500 cm⁻¹. The peak at 70 cm⁻¹ is attributed to acoustic phonons, while the 330 and 500 cm^{-1} peaks are assigned to A_{2u} and A_{1g} optical modes. In addition, the small peak at around $830\ cm^{-1}$ originates from the LO phonon at the X-point.

Phonon excitation also affects the band gap and exciton binding energy (60). As shown in Table 1, when temperature is increased from 0 K to 300 K, the direct QP band gap has a blueshift of 70 meV, while the indirect QP band gap has a redshift of 50 meV. The optical band gap corresponding to the bright exciton has a blueshift

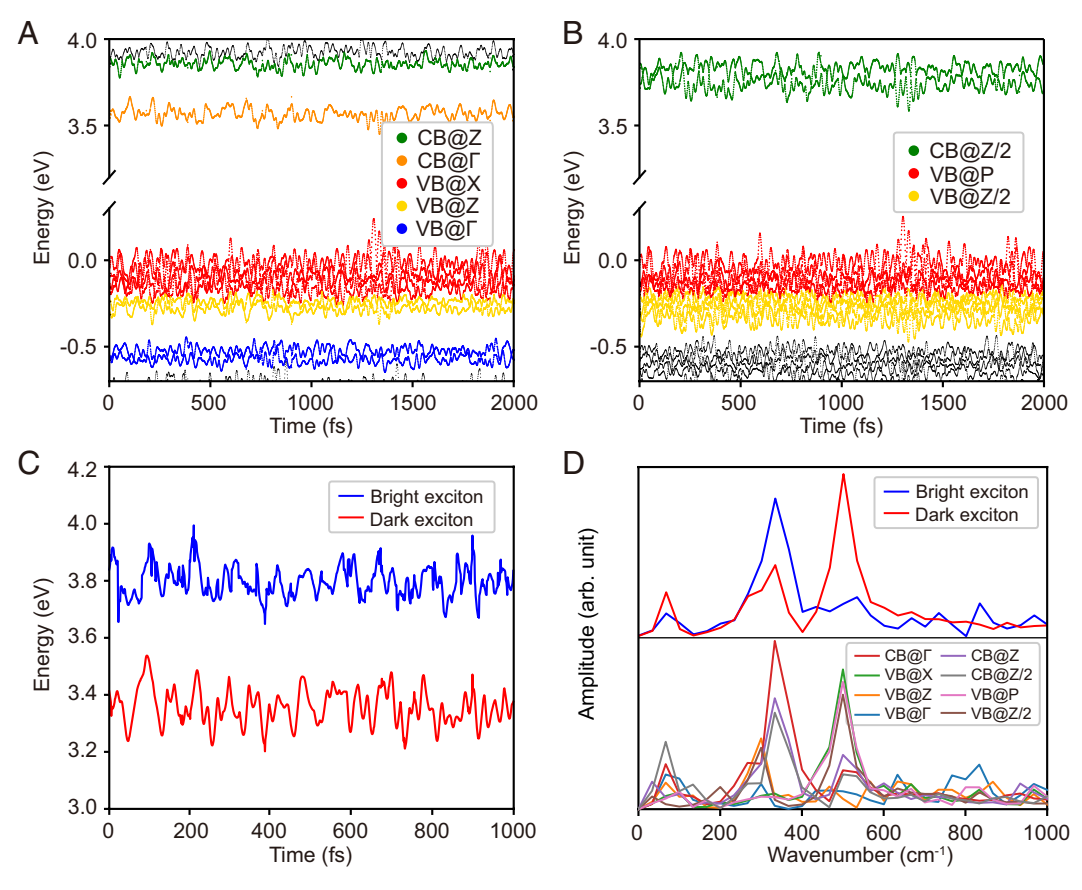


Fig. 3. Time-dependent energy evolution of the QP (*A* and *B*) and exciton (*C*) energies and their FT spectra (*D*) at 300 K. The energy reference in *A* and *B* is that of the averaged VBM.

of 100 meV. Baldini et al. observed a 40-meV blueshift of the optical band gap when the temperature increased from 20 to 300 K, which is in line with our calculation. The binding energy for the bright exciton decreases to 194 meV, while change in the binding energy for the dark exciton is negligible. Therefore, the bright and dark excitons have very similar binding energies at room temperature.

Bright-Dark Exciton Transition. To simulate the bright-dark exciton dynamics, we choose a representative exciton state at approximately 3.7 eV at the major peak of exciton absorption as the initial state. As shown in Fig. 4, the largest component of the initial exciton is the Z/2-Z/2 component, which has an approximately 30% contribution. The direct e-h pairs at $\mathbb{Z}/4$ - $\mathbb{Z}/4$ and 3Z/4-3Z/4 and indirect *e-h* pairs at Z/2-P also contribute. Fig. 4A shows the time-dependent exciton population projected on different e-h pairs. It can be seen that the population on $\mathbb{Z}/2$ - $\mathbb{Z}/2$ decreare to zero in the first 100 fs. The Z/2-P component increases from 10% to 20% in the first 20 fs and then also decreases to zero in the first 100 fs. Subsequently, the Z/4-Q component increases from 2% to 25% in the first 70 fs and then slowly decreases to less than 10% within 200 fs. In the same period, the Γ -X component increases from zero to approximately 60%, as the equilibrium is reached. By fitting the decreasing curve of Z/2-Z/2 and increasing curve of Γ -X, we obtain the respective timescales of 34 and 81 fs.

The exciton relaxation pathway is determined by the NAC between different e-h pairs, which includes the contribution by e-ph interaction, the Coulomb interaction W, and exchange interaction v_{ex} , according to Eqs. 1 and 6 in *Materials and Methods*. Fig. 5A shows the total NAC elements averaged over the AIMD trajectory, while Fig. 5B-D display the individual contributions by W, v_{ex} , and e-ph, respectively. The color bar indicates the magnitude of NACs. One can see that v_{ex} and W have a similar law of change, but v_{ex} is two orders of magnitude smaller than W, suggesting that the contribution of the exchange interaction can be neglected. W, however, has a comparable effect to the e-ph interaction. It can be seen from Fig. 5A that for the Z/2-Z/2 e-h pair,

the NAC with Z/2-P is the largest, which stimulates the fast transition from Z/2-Z/2 to Z/2-P in the first 20 fs. Then, Z/2-P has a relatively large NAC with Z/4-Q, leading to the transition from Z/2-P to Z/4-Q. It also has a small probability of transferring to Γ -X directly. Finally, the Z/4-Q *e-h* pair will relax to Γ -X due to the large NAC. Thus, we can determine the major exciton transition pathway as $(Z/2-Z/2)-(Z/2-P)-(Z/4-Q)-(\Gamma-X)$. In addition, there is a minor exciton transition pathway as $(Z/2-Z/2)-(Z/2-P)-(\Gamma-X)$. From Fig. 5 *B-D*, one can see that the first step (Z/2-Z/2)-(Z/2-P) is motivated by *e-ph* coupling, and the other exciton transformations are driven by the many-body Coulomb interaction *W*. A schematic diagram of the exciton transition path from Z/2-Z/2 to Γ -X is summarized in Fig. 4*C*.

We have also studied the exciton transition by setting the initial exciton at approximately 3.85 eV, where a small peak mainly contributed by Γ - Γ *e-h* pair shows up in the absorption spectra. Choosing such an initial state is easy to compare with the single-particle hole scattering process from Γ to X. The exciton dynamics results are shown in Fig. 4D. Compared to the averaged NAC elements, the major exciton transition pathway can be determined as $(\Gamma-\Gamma)$ – (Z/4-Z/4) – (Z/4-Q) – $(\Gamma-X)$, whereas the $(\Gamma-\Gamma)$ $-(\Gamma-X)$ transition plays a minor role, as schematically shown in Fig. 4F. The timescales for Γ - Γ decreasing and Γ -X increasing are 43 and 85 fs, respectively. The *e-ph* interaction is dominant in the minor transition path $(\Gamma-\Gamma)$ – $(\Gamma-X)$, and the Coulomb interaction W plays the dominant role in the major exciton transition pathway. From Fig. 5, one can see that the *e-ph*-induced NAC between Γ -X and Γ -Z is large, which is due to the small energy difference between VB@Z and VB@X. Despite the large NAC between Γ-X and Γ -Z, the coupling between $\hat{\Gamma}$ -Z with other *e-h* pairs are relatively small. Therefore, Γ -Z does not play a dominating role in the major exciton relaxation route from $\mathbb{Z}/2$ - $\mathbb{Z}/2$ or Γ - Γ to Γ - \mathbb{X} .

The momentum-resolved dynamics results affirm that the many-body effects play a crucial role in the exciton relaxation dynamics of anatase ${\rm TiO_2}$. For further understanding, we use the single-particle TDKS-NAMD method to investigate the *e-h*

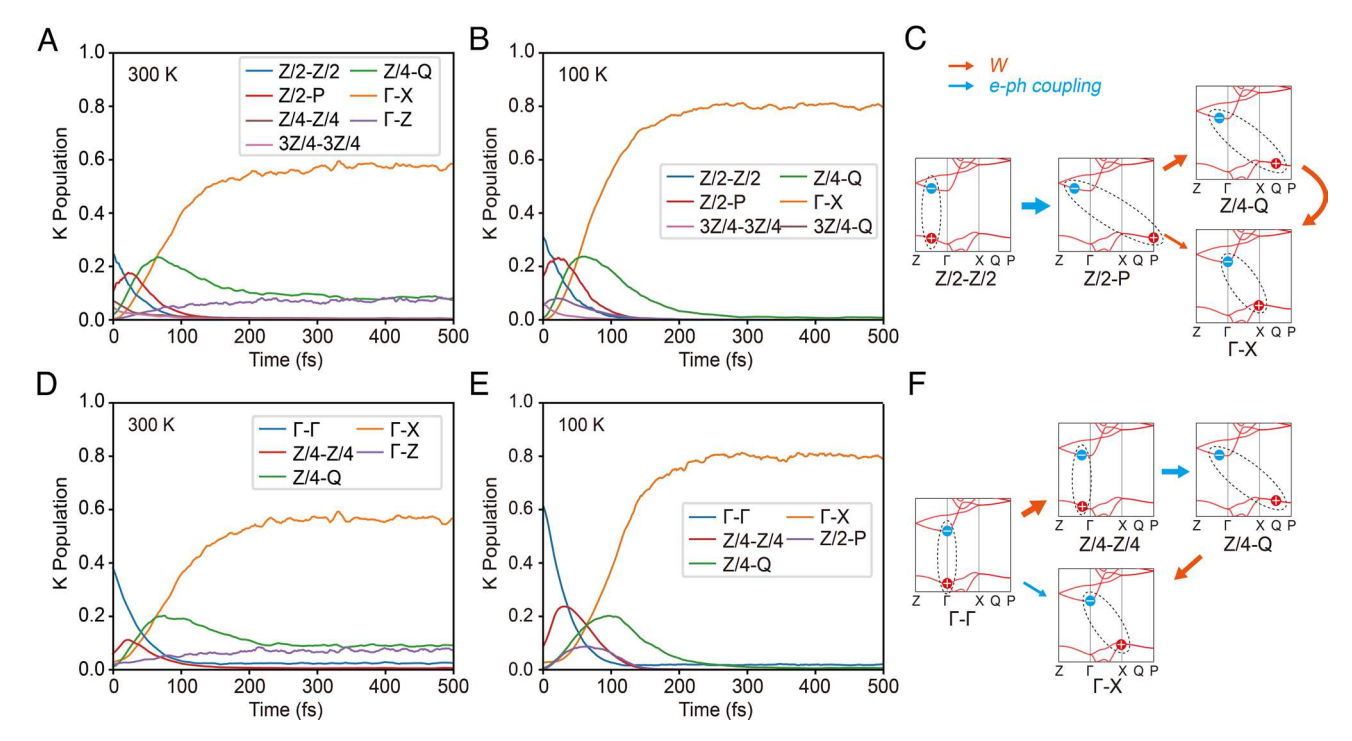


Fig. 4. Time evolution of the population on major e-h pairs and the schematic diagram of the exciton dynamics channels with different initial exciton states (Z/2-Z/2: A-C and Γ - Γ : D-F) at 300 K (A and A) and 100 K (B and A). Red and blue arrows in A and A represent the contributions of A0 and A1 and A2 and A3 and A3 and A4 and A5.

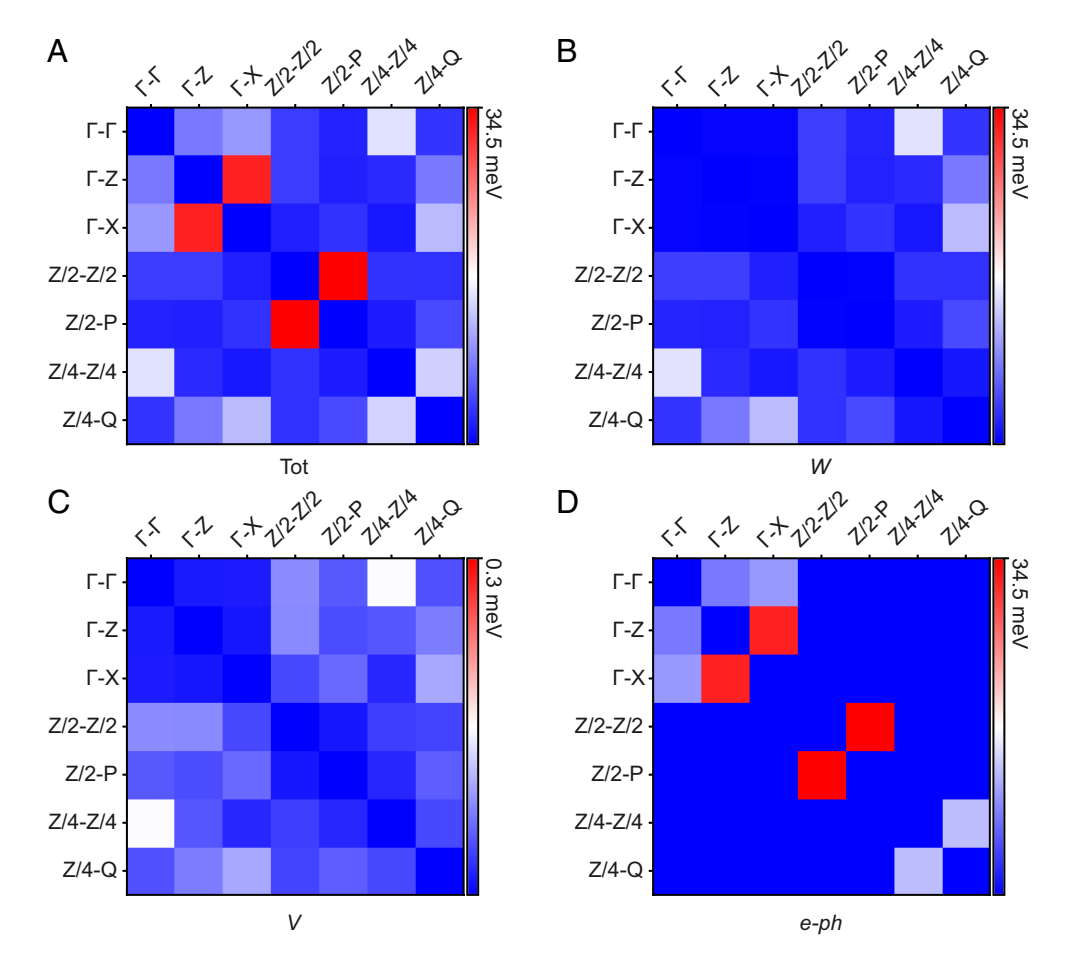


Fig. 5. Distribution of total NAC (A), and the contribution from W(B), $v_{ex}(C)$, and e-ph coupling (D) averaged over the AIMD trajectory between different e-h pairs at 300 K.

pair relaxation process from Γ - Γ to Γ -X. Ignoring the e-h interaction, this process is equivalent to hole scattering from Γ to X stimulated by e-ph scattering. In this case, because the hole energy at Z is between the Γ point and the X point, hole scattering can occur among Γ , Z, and X points, and the NACs shown in the *Inset* of Fig. 6A are contributed by e-ph coupling. Direct $(\Gamma$ - Γ) – $(\Gamma$ -X) is the major route, and $(\Gamma$ - Γ) – $(\Gamma$ -Z) – $(\Gamma$ -X) is a minor route. Since the NAC between X and Z is quite large, the hole relaxes very fast from Z to X. Therefore, we hardly see a temporary occupation of Z point in Fig. 6. Since the many-body e-h interaction is not included, e-ph coupling defines the hole

relaxation. The timescale of hole scattering from Γ to X is approximately 300 fs, which is slower than the exciton relaxation because all the relaxation mediated by the many-body interaction is suppressed.

In general, the magnitude of *e-ph* coupling is influenced by temperature, but the relationship between many-body effects and temperature is still unclear. In order to gain a deeper understanding of this point, we study the bright–dark exciton transition process at 100 K. The time-dependent QP and exciton energies along the AIMD trajectory at 100 K and their FT spectra are shown in *SI Appendix*, Fig. S5. Compared to the results

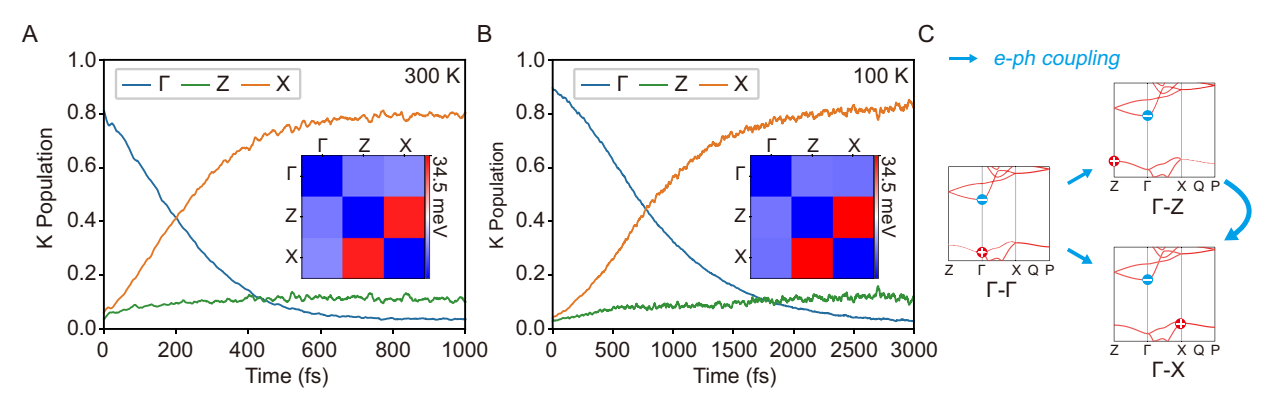


Fig. 6. Time evolution of the hole population at 300 K (*A*) and 100 K (*B*) and schematic diagram of the hole dynamics channel (*C*). The *Inset* shows the NAC between different KS states, which is contributed by the *e-ph* coupling.

at 300 K (Fig. 3), the energy fluctuation of the QP and exciton energy at 100 K are not as pronounced. The FT spectra show that only the A_{2u} phonon mode at 330 cm⁻¹ plays a dominant role at 100 K. All these results suggest a weaker exciton excitation and electron-phonon coupling at 100 K. The results of brightdark exciton transition are shown in Fig. 4 B and E. The corresponding NACs between different e-h pairs are shown in SI Appendix, Figs. S3 and S6. Compared to the results at 300 K, one can see that the bright-dark exciton transition at 100 K occurs on similar timescales. The major transition pathways are also the same. The most distinct difference is that the temperature decrease suppresses the *e-ph* coupling between Γ - Γ and Γ -X(10.3 to 7.6 meV) but enhances the many-body Coulomb interaction induced coupling between Γ - Γ and Z/4-Z/4 (15.3 to 23.8 meV). The enhancement of the W term may be associated with the small atomic structure change by phonon freezing at 100 K. Thus, when Γ - Γ *e-h* pair is set as the initial state, the W derived exciton transition route $(\Gamma - \Gamma) - (Z/4 - Z/4) - (Z/4 - Q) - (\Gamma - X)$ plays a more dominating role compared to the *e-ph* leading $(\Gamma - \Gamma)$ $(\Gamma$ -X) path at 100 K.

To further understand the role of many-body effects, we also simulate the single-particle hole scattering process at 100 K. The results are shown in Fig. 6B. It can be seen that since the e-ph coupling of Γ -X and Γ -Z are suppressed as the temperature decreases, the timescale of hole scattering from Γ to X extends to 800 fs. Therefore, we can further conclude that the many-body effects play a crucial role in the fast bright-dark exciton transition at low temperature.

Discussion

Until now, there has been no direct time-resolved measurement that can be directly compared with the GW + rtBSE-NAMD simulation. Experimental measurements of the bright exciton decay and the dark exciton risetime are both challenging. The lifetime of bright excitons, however, can be estimated from the experimental width of its absorption spectra. Baldini et al. obtained an absorption peak with a width of approximately 200 meV at 300 K, which if interpreted as uncertainty broadening corresponds to a 3-fs decoherence time (12). The linewidth is closer to that expected from the many-body exciton relaxation timescale than the single-particle relaxation timescale. The broader linewidth, suggests that it is affected by factors other than energy and momentum scattering that affect the exciton coherent quantum dynamics. For example, in the simulation, we chose one exciton state as an initial state. In the experiments, multiexciton states can be excited. As a n-type semiconductor, the defects contributed by oxygen vacancy and interstitial Ti generally exist (61-63). The exciton-defect scattering may affect the exciton dynamics. In addition, it is known that the large polaron can be formed in anatase TiO₂ (64), which can change the dielectric environment. Finally, the electron-electron scattering is not considered in the simulation, which also may be a factor contributing to the experimental linewidth.

The GW + rtBSE-NAMD method predicts that when the electron and hole are bound together, forming an exciton, the e-h interaction leads to additional relaxation channels compared to those of single particles, which can significantly accelerate exciton relaxation process. The NAMD simulation based on LR-TDDFT, which can also capture the exciton character, suggests that exciton effects accelerate charge relaxation in different systems (65). In our previous GW + rtBSE-NAMD study on MoS₂, we found that the e-h exchange interaction enhances spin-valley depolarization (50). Here, by contrast, the exciton in anatase is not spin-polarized,

and we reveal that the screened Coulomb interaction plays the dominant role in the carrier energy and momentum scattering. The Coulomb interaction plays a vital role in anatase, and by extension to other indirect solid systems, where it not only influences the bright exciton energy, but also shortens its lifetime leading to formation of the band gap dark excitons.

In the applications to light harvesting, anatase TiO₂ is known to enable energy transduction with high conversion efficiency (62, 66, 67). The existence of bright exciton ensures good light absorption properties in the near-UV spectral region. After the e-h pair forms a bright exciton, our work suggests that instead of e-h recombination, they undergo ultrafast relaxation to form indirect dark excitons. The momentum-forbidden indirect dark exciton is expected to have a longer lifetime than the direct e-h pair, which favors the photocatalytic activity of anatase TiO₂.

The role of many-body e-h Coulomb interactions suggests that the exciton dynamics will strongly depend on the electron and hole density, which can be controlled by the photoexcitation or the doping density. The effect of high carrier density is not known and needs to be investigated. On one hand, high carrier density can affect the e-h Coulomb interactions, and thus accelerate the bright exciton transformation, and on the other hand, reduce the exciton binding, with untested effect on the dark exciton population and lifetimes. The present GW + rtBSE-NAMD simulation has been performed for single e-h pair excitation but can be extended to investigate the effect of electron or hole doping. Moreover, if one considers dark excitons as carriers of quantum information, GW + rtBSE-NAMD methods can be used to investigate their decoherence by momentum scattering. The same methods can be extended to 2D quantum materials, to analyze their spin and valley scattering, as well as semiconductors with potentially interesting optically dressed topological properties (68, 69). The example of anatase TiO₂ dark exciton formation is an unappreciated example of optically induced metastable phase formation, that is capable of transduction of light to chemical energy. Anatase is also known to form electron polarons (70), which have not been considered in the present calculations. It would also be interesting to extend the simulations to investigate the effect of polaron response on screening of the Coulomb interaction on the exciton binding energy and bright-dark transformation.

In conclusion, by using the GW + rtBSE-NAMD method, we have investigated the bright-dark exciton transition in anatase TiO₂. First, based on the GW + rtBSE-NAMD approach, the decay of bright excitons to form Γ -X momentum-forbidden dark excitons can be investigated with energy, momentum, and time resolution. The binding energy of dark excitons is large, similar to that of the bright exciton, which identifies it as the catalytically active species in photocatalysis. GW + rtBSE-NAMD simulation suggests that the bright-dark exciton transition occurs in an ultrafast manner in 100 fs. Interestingly, the bright-dark exciton transition does not occur dominantly by e-ph coupling. Instead, many-body e-h Coulomb interactions activate additional fast relaxation channels and distinctly accelerate exciton relaxation. The insights into the dark exciton formation and ultrafast bright-dark exciton transition in anatase TiO2 will be critical for advancing its applications in optoelectronic devices and light-energy harvesting.

Materials and Methods

GW+BSE for the Properties of the Dark Exciton. A G_0W_0 calculation based on the DFT Kohn-Sham (KS) wavefunctions using the Perdew-Burke-Ernzerhof (PBE) functional (G₀W₀@PBE) (71) is performed using a primitive cell with 8 \times 8 \times 8 k-points by the Vienna Ab initio Simulation Package (VASP) (72-74). The BSE calculation is performed with the self-developed Hefei-NAMD code (50, 52), where GW + rtBSE-NAMD is implemented. The BSE Hamiltonian is constructed as

$$\left\langle \mathbf{k}cv|H|\mathbf{k}'c'v'\right\rangle = \left(E_{\mathbf{k}c}^{QP} - E_{\mathbf{k}v}^{QP}\right)\delta_{\mathbf{k}\mathbf{k}'}\delta_{cc'}\delta_{vv'} - W_{\mathbf{k}'c'v'}^{\mathbf{k}cv} + V_{ex}^{\mathbf{k}cv}V_{ex}^{\mathbf{k}c'}V_{ex}^{$$

where v/c represents the index of the valance hole and conduction electron, and $E_{kv}^{\rm QP}$ and $E_{kv}^{\rm QP}$ are their G_0W_0 QP energies. $|\mathbf{k}cv\rangle = \Psi_{\mathbf{k}c}(\mathbf{r}_e)\Psi_{\mathbf{k}v}^*(\mathbf{r}_h)$ is the e-h pair basis set. W and v_{ex} represent the screened Coulomb and exchange interaction between the electron and hole, respectively, which can be written as

$$\begin{split} W_{\mathbf{k}'c'v'}^{\mathbf{k}cv} &= \frac{1}{\Omega} \sum_{\mathbf{G}\mathbf{G}'} \frac{4\pi\varepsilon_{\mathbf{G}\mathbf{G}'}^{-1} \left(\mathbf{k} - \mathbf{k}'\right)}{\left|\mathbf{k} - \mathbf{k}' + \mathbf{G}\right| \left|\mathbf{k} - \mathbf{k}' + \mathbf{G}'\right|} \left(\beta_{\uparrow \mathbf{k}'c'}^{\uparrow \mathbf{k}c}(\mathbf{G}) + \beta_{\downarrow \mathbf{k}'c'}^{\downarrow \mathbf{k}c}(\mathbf{G})\right) \\ &\left(\beta_{\uparrow \mathbf{k}'v'}^{\uparrow \mathbf{k}v*} \left(\mathbf{G}'\right) + \beta_{\downarrow \mathbf{k}'v'}^{\downarrow \mathbf{k}v*}(\mathbf{G}')\right), \end{split} \tag{2}$$

$$v_{ex\,\mathbf{k}'c'v'}^{\mathbf{k}cv} = \frac{1}{\Omega} \sum_{\mathbf{G} \neq \mathbf{0}} \frac{4\pi}{|\mathbf{G}|^2} \left(B_{\uparrow\mathbf{k}v}^{\uparrow\mathbf{k}c}(\mathbf{G}) + B_{\downarrow\mathbf{k}v}^{\downarrow\mathbf{k}c}(\mathbf{G}) \right) \left(B_{\uparrow\mathbf{k}'v'}^{\uparrow\mathbf{k}'c'*}(\mathbf{G}) + B_{\downarrow\mathbf{k}'v'}^{\downarrow\mathbf{k}'c'*}(\mathbf{G}) \right).$$
[3

Here, $\boldsymbol{\varepsilon}_{\mathbf{GG'}}^{-1}(\mathbf{k}-\mathbf{k'})$ is the inverse dielectric function from the G_0W_0 calculation using random phase approximation (RPA) (75, 76). \mathbf{G} is the reciprocal lattice vector, and the Bloch integral, B, is defined as $B_{\sigma \mathbf{k'}n'}^{\mathbf{k}n}(\mathbf{G}) = \left\langle u_{\sigma \mathbf{k}n} \mid e^{i\mathbf{G}\mathbf{r}} \mid u_{\sigma \mathbf{k'}n'} \right\rangle$, and is calculated from the KS basis sets. The exciton energy and exciton wavefunctions are obtained by diagonalization of the BSE Hamiltonian. To calculate the binding energy of dark excitons, we establish a $2 \times 2 \times 1$ conventional supercell to perform the BSE calculation with $4 \times 4 \times 4$ k-points. This enables the X point, near the VBM in momentum space, to be folded into the Γ point. The three lowest CBs and eight topmost VBs are included to solve the excitonic Hamiltonian. To verify the reliability of the self-developed BSE approach, we compare our calculated bright exciton energies to those reported in ref. 12, as shown in Table 1, and find good consistency.

Bright-Dark Exciton Transition According to GW + rtBSE-NAMD. The GW + rtBSE-NAMD is an extension of single-particle ab initio nonadiabatic molecular dynamics based on the time-dependent Kohn-Sham equation (TDKS-NAMD). It combines GW+BSE with real-time NAMD simulation using the surface hopping scheme (77) and classical path approximation (CPA) (78). In this approach, the real-time BSE Hamiltonian needs to be constructed from the time-dependent W and v_{ex} terms, as well as the QP energies, as expressed in Eq. 1. Based on CPA, the trajectory of the nuclear motion $\mathbf{R}(t)$ is predetermined by ab initio molecular dynamics (AIMD). Based on the AIMD trajectory, the time-dependent KS basis sets can be obtained to calculate the exchange term v_{ex} as expressed in Eq. 3. During the AIMD simulation, the rigid dielectric function approximation is used, under the assumption that it remains unchanged by molecular dynamics (50). The inverse dielectric function $\varepsilon_{\mathbf{GG'}}^{-1}(\mathbf{k}-\mathbf{k'})$ is obtained from the single-point G_0W_0 calculation with a primitive cell, and the screened Coulomb term W is calculated using the inverse dielectric function and time-dependent KS orbitals, as indicated in Eq. **2**. Finally, the energy difference $\Delta E_{\text{GW-PBE}}$ between the QP energies from the single-point G_0W_0 calculation using the primitive cell and KS energies using the PBE functional is obtained. The QP energies along the AIMD trajectory are obtained using the scissor operator by adding $\Delta E_{\text{GW-PBE}}$ to the PBE KS energies. The real-time BSE Hamiltonian is constructed with W, v_{ex} , and QP energies. From that, the time-dependent two-particle Schrödinger equation follows

$$i\hbar \frac{\partial \Phi(\mathbf{r}_{e}, \mathbf{r}_{h}, t)}{\partial t} = H(\mathbf{R}(t))\Phi(\mathbf{r}_{e}, \mathbf{r}_{h}, t).$$
 [4]

In the e-h pair basis set, the excited state wavefunction is written as

$$\Phi(\mathbf{r}_{e},\mathbf{r}_{h},t) = \sum_{\mathbf{k}} \sum_{c}^{\text{elec}} \sum_{v}^{\text{hole}} A_{\mathbf{k}cv}(t) \Psi_{\mathbf{k}c}(\mathbf{r}_{e}) \Psi_{\mathbf{k}v}^{*}(\mathbf{r}_{h}), \quad [5]$$

where $\Psi_{\mathbf{k}c}(\mathbf{r}_e)$ and $\Psi_{\mathbf{k}v}^*(\mathbf{r}_h)$ are the KS orbitals of the electron and hole. The time evolution of the coefficient $A_{\mathbf{k}cv}(t)$ is expressed as

 $i\hbar\dot{A}_{\mathbf{k}\alpha}(t) =$

$$\sum_{\mathbf{k}'} \sum_{c'}^{\text{elec}} \sum_{v'}^{\text{hole}} \left(\left\langle \mathbf{k} c v | H | \mathbf{k}' c' v' \right\rangle - i \hbar \left\langle \mathbf{k} c v \left| \frac{\partial}{\partial t} \right| \mathbf{k}' c' v' \right\rangle \right) A_{\mathbf{k}' c' v'}(t),$$
[6

where $\langle \mathbf{k}cv \mid H \mid \mathbf{k}' c' v' \rangle$ is the BSE Hamiltonian. In this representation, the excited state is described as an e-h pair by KS orbitals.

The solution of Eq. **6** describes the coherent time evolution of excitonic states coupled to the nuclear subsystems, which is expressed by a superposition of different basis sets. Such a superposition is not measurable because a quantum mechanical measurement projects it onto just one pure state. Similar to previous studies, stochastic surface hopping can be applied to the system to overcome this limitation. Specifically, we use the fewest switches surface hopping (FSSH) scheme developed by Tully (77). Within the framework of surface hopping, the nonadiabatic coupling elements (NACs) fdetermine the hopping or transition probability from one quantum state to another. In the TDKS-NAMD method, the NAC is calculated as (79)

$$d_{jk} = \frac{\left\langle \Psi_{j}^{KS} \middle| \nabla_{\mathbf{R}} H \middle| \Psi_{k}^{KS} \middle\rangle}{E_{j}^{KS} - E_{k}^{KS}} \dot{\mathbf{R}} = \left\langle \Psi_{j}^{KS} \middle| \frac{\partial}{\partial t} \middle| \Psi_{k}^{KS} \middle\rangle, \tag{7}$$

in which Ψ_j^{KS} and Ψ_k^{KS} are the KS orbitals, and E_j^{KS} and E_k^{KS} are the KS energies. The e-ph interaction $\left\langle \Psi_j^{\text{KS}} \mid \nabla_{\mathbf{R}} H \mid \Psi_k^{\text{KS}} \right\rangle$ is captured in the NAC from the KS evolution along with the AIMD.

In the GW + rtBSE - NAMD approach, the NAC includes the off-diagonal elements of

$$\langle \mathbf{k} c v | H | \mathbf{k}' c' v' \rangle - i \hbar \langle \mathbf{k} c v | \frac{\partial}{\partial t} | \mathbf{k}' c' v' \rangle$$
, [8]

in Eq. 6 where

$$\left\langle \mathbf{k}cv \left| \frac{\partial}{\partial t} \right| \mathbf{k}'c'v' \right\rangle =$$

$$\left\{ \left(\left\langle \uparrow \mathbf{k}c \left| \frac{\partial}{\partial t} \right| \uparrow \mathbf{k}c' \right\rangle + \left\langle \downarrow \mathbf{k}c \left| \frac{\partial}{\partial t} \right| \downarrow \mathbf{k}c' \right\rangle \right) \delta_{vv'} \right\} \delta_{kk'} \cdot$$

$$\left\{ + \left(\left\langle \uparrow \mathbf{k}v \left| \frac{\partial}{\partial t} \right| \uparrow \mathbf{k}v' \right\rangle + \left\langle \downarrow \mathbf{k}v \left| \frac{\partial}{\partial t} \right| \downarrow \mathbf{k}v' \right\rangle \right)^* \delta_{cc'} \right\} \delta_{kk'} \cdot$$
[9

This equation jointly includes the e-ph interaction contributed by both the electron and the hole, as an extension of NAC in TDKS-NAMD. In addition to the e-ph part shown in Eq. $\bf 9$, $\langle {\bf k} cv \mid H \mid {\bf k}' c' \ v' \rangle$ contains the off-diagonal contributions from W and v_{ex} (Eqs. $\bf 2$ and $\bf 3$) that are included in NAC. Their inclusion reveals that they play a crucial role in the bright-dark exciton transition in anatase TiO₂, as discussed above.

Data, Materials, and Software Availability. The code can be downloaded at the following GitHub, https://github.com/realxiangjiang/paraHFNAMD (80). All data associated with this study can be downloaded at the following GitHub, https://github.com/AoleiWang/Datasets-of-Anatase-TiO2 (81). All other data are included in the manuscript and/or *SI Appendix*.

ACKNOWLEDGMENTS. J.Z. acknowledges the support of Strategic Priority Research Program of the Chinese Academy of Sciences, grant no. XDB0450101, Innovation Program for Quantum Science and Technology 2021ZD0303306; NSFC, grant nos. 12125408 and 11974322; and the informatization plan of Chinese Academy of Sciences, grant no. CASWX2021SF-0105. Q.Z. acknowledges the support of the National Natural Science Foundation of China (NSFC), grant no. 12174363. Calculations were performed at Hefei Advanced Computing Center, Supercomputing Center at USTC, and ORISE Supercomputer. H.P. acknowledges support from the NSF grant CHE-2102601.

- W. Brütting, "Introduction to the physics of organic semiconductors" in *Physics of Organic Semiconductors*, W. Brütting, Ed. (John Wiley & Sons Ltd, 2005), pp. 1–14.
- A. Classen et al., The role of exciton lifetime for charge generation in organic solar cells at negligible energy-level offsets. Nat. Energy 5, 711-719 (2020).
- J. Sneyd Alexander *et al.*, Efficient energy transport in an organic semiconductor mediated by transient exciton delocalization. *Sci. Adv.* **7**, eabh4232 (2021).
- H. Kunugita et al., Excitonic feature in hybrid perovskite CH₃NH₃PbBr₃ single crystals. Chem. Lett. **44**, 852-854 (2015).
- L. M. Herz, Charge-carrier dynamics in organic-inorganic metal halide perovskites. Annu. Rev. Phys.
- Chem. 67, 65-89 (2016). M. Baranowski, P. Plochocka, Excitons in metal-halide perovskites. Adv. Energy Mater. 10, 1903659
- J. R. Schaibley et al., Valleytronics in 2D materials. Nat. Rev. Mater. 1, 16055 (2016).
- 8. G. Wang et al., Colloquium: Excitons in atomically thin transition metal dichalcogenides. Rev. Mod. Phys. 90, 021001 (2018).
- P. Rivera et al., Interlayer valley excitons in heterobilayers of transition metal dichalcogenides. Nat. Nanotechnol. 13, 1004-1015 (2018).
- C. Klingshirn, R. Hauschild, J. Fallert, H. Kalt, Room-temperature stimulated emission of ZnO: Alternatives to excitonic lasing. Phys. Rev. B 75, 115203 (2007).
- P. K. Gogoi et al., Anomalous excitons and screenings unveiling strong electronic correlations in $SrTi_{1,y}Nb_yO_3$ (0 $\leq x \leq 0.005$). Phys. Rev. B **92**, 035119 (2015).
- E. Baldini et al., Strongly bound excitons in anatase TiO₂ single crystals and nanoparticles. Nat. Commun. 8, 13 (2017).
- S. Biswas, J. Husek, S. Londo, L. R. Baker, Highly localized charge transfer excitons in metal oxide
- semiconductors. Nano Lett. **18**, 1228–1233 (2018). E. Rabani, R. Baer, Theory of multiexciton generation in semiconductor nanocrystals. *Chem. Phys.* Lett. 496, 227-235 (2010).
- D. Snoke, P. Littlewood, Polariton condensates. Phys. Today 63, 42–47 (2010).
- T. Mueller, E. Malic, Exciton physics and device application of two-dimensional transition metal dichalcogenide semiconductors. npj 2D Mater. Appl. 2, 29 (2018).
- E. Malic et al., Dark excitons in transition metal dichalcogenides. Phys. Rev. Mater. 2, 014002
- R. Wallauer et al., Momentum-resolved observation of exciton formation dynamics in monolayer WS₂. Nano Lett. 21, 5867-5873 (2021).
- E. Poem et al., Accessing the dark exciton with light. Nat. Phys. 6, 993-997 (2010).
- Z. Ye et al., Probing excitonic dark states in single-layer tungsten disulphide. Nature 513, 214-218
- X.-X. Zhang, Y. You, S. Y. F. Zhao, T. F. Heinz, Experimental evidence for dark excitons in monolayer WSe2. Phys. Rev. Lett. 115, 257403 (2015).
- T. Smoleński, T. Kazimierczuk, M. Goryca, P. Wojnar, P. Kossacki, Mechanism and dynamics of biexciton formation from a long-lived dark exciton in a CdTe quantum dot. Phys. Rev. B 91, 155430 (2015)
- X.-X. Zhang et al., Magnetic brightening and control of dark excitons in monolayer WSe2. Nat. Nanotechnol. 12, 883-888 (2017).
- L. Wu, Y. Chen, H. Zhou, H. Zhu, Ultrafast energy transfer of both bright and dark excitons in 2D van der Waals heterostructures beyond dipolar coupling. ACS Nano 13, 2341-2348 (2019).
- J. Madéo et al., Directly visualizing the momentum-forbidden dark excitons and their dynamics in atomically thin semiconductors. Science 370, 1199-1204 (2020).
- Q. Zheng et al., Phonon-assisted ultrafast charge transfer at van der Waals heterostructure interface. Nano Lett. 17, 6435-6442 (2017).
- V. Kumar, N. Narwal, M. Kumar, Temporal-spatial-energy resolved advance multidimensional techniques to probe photovoltaic materials from atomistic viewpoint for next-generation energy solutions. Energy Environ. Sci. 14, 4760-4802 (2021).
- 28. A. Fujishima, K. Honda, Electrochemical photolysis of water at a semiconductor electrode. Nature 238, 37-38 (1972).
- E. Pelizzetti, C. Minero, Mechanism of the photo-oxidative degradation of organic pollutants over TiO₂ particles. Electrochim. Acta 38, 47-55 (1993)
- T. L. Thompson, J. T. Yates, Surface science studies of the photoactivation of TiO₂ new photochemical processes. Chem. Rev. 106, 4428-4453 (2006).
- A. Fujishima, X. Zhang, D. A. Tryk, TiO₂ photocatalysis and related surface phenomena. *Surf. Sci. Rep.* 63, 515-582 (2008)
- M. Setvín et al., Reaction of O_2 with subsurface oxygen vacancies on TiO_2 anatase (101). Science 341, 988-991 (2013).
- J. Yu, J. Low, W. Xiao, P. Zhou, M. Jaroniec, Enhanced photocatalytic CO₂-reduction activity of anatase TiO₂ by Coexposed 001 and 101 Facets. J. Am. Chem. Soc. 136, 8839–8842 (2014).
- J. Schneider et al., Understanding TiO₂ photocatalysis: Mechanisms and materials. Chem. Rev. 114, 9919-9986 (2014).
- M. Grätzel, Photoelectrochemical cells. Nature 414, 338-344 (2001).
- D. He et al., Micro fiber with cladding of titanium dioxide (TiO₂) nanoparticles and its violet light sensing. Opt. Mater. Express 7, 264–272 (2017).
- B. O'Regan, M. Grätzel, A low-cost, high-efficiency solar cell based on dye-sensitized colloidal TiO₂ films. Nature 353, 737-740 (1991).
- J. Bai, B. Zhou, Titanium dioxide nanomaterials for sensor applications. Chem. Rev. 114, 10131-10176 (2014).
- M. Freitag et al., Dye-sensitized solar cells for efficient power generation under ambient lighting. Nat. Photonics 11, 372-378 (2017).
- E. Baldini et al., Exciton control in a room temperature bulk semiconductor with coherent strain pulses. Sci. Adv. 5, eaax2937 (2019).

- 41. M. Emori, M. Sugita, K. Ozawa, H. Sakama, Electronic structure of epitaxial anatase TiO₂ films: Angleresolved photoelectron spectroscopy study. Phys. Rev. B 85, 035129 (2012).
- L. Chiodo et al., Self-energy and excitonic effects in the electronic and optical properties of TiO₂ crystalline phases. Phys. Rev. B 82, 045207 (2010).
- M. S. Hybertsen, S. G. Louie, Electron correlation in semiconductors and insulators: Band gaps and quasiparticle energies. Phys. Rev. B 34, 5390-5413 (1986).
- M. Rohlfing, S. G. Louie, Electron-hole excitations and optical spectra from first principles. Phys. Rev. B 62, 4927-4944 (2000).
- G. Onida, L. Reining, A. Rubio, Electronic excitations: Density-functional versus many-body Green'sfunction approaches. *Rev. Mod. Phys.* **74**, 601–659 (2002).

 A. Ramasubramaniam, Large excitonic effects in monolayers of molybdenum and tungsten
- dichalcogenides. Phys. Rev. B 86, 115409 (2012).
- L. Yang, M. L. Cohen, S. G. Louie, Excitonic effects in the optical spectra of graphene nanoribbons. Nano Lett. 7, 3112-3115 (2007).
- C.-H. Park, S. G. Louie, Tunable excitons in biased bilayer graphene. Nano Lett. 10, 426-431 (2010).
- H. Sun et al., Comparing quasiparticle H₂O level alignment on anatase and rutile TiO₂. ACS Catal. 5, 4242-4254 (2015).
- X. Jiang et al., Real-time GW-BSE investigations on spin-valley exciton dynamics in monolayer transition metal dichalcogenide. Sci. Adv. 7, eabf3759 (2021).
- W. Setyawan, S. Curtarolo, High-throughput electronic band structure calculations: Challenges and tools. Comput. Mater. Sci 49, 299-312 (2010).
- Q. Zheng et al., Ab initio nonadiabatic molecular dynamics investigations on the excited carriers in condensed matter systems. WIREs Comput. Mol. Sci. 9, e1411 (2019).
- B. Monserrat, Correlation effects on electron-phonon coupling in semiconductors: Many-body theory along thermal lines. *Phys. Rev. B* **93**, 100301 (2016). H. Tang, H. Berger, P. E. Schmid, F. Lévy, Optical properties of anatase (TiO₂). *Solid State Commun.*
- 92, 267-271 (1994).
- H. Tang, K. Prasad, R. Sanjinès, P. E. Schmid, F. Lévy, Electrical and optical properties of TiO_2 anatase thin films. *J. Appl. Phys.* **75**, 2042–2047 (1994).
- W. Kang, M. S. Hybertsen, Quasiparticle and optical properties of rutile and anatase TiO₂. Phys. Rev. B82, 085203 (2010).
- F. De Angelis, C. Di Valentin, S. Fantacci, A. Vittadini, A. Selloni, Theoretical studies on anatase and less common TiO₂ Phases: Bulk, surfaces, and nanomaterials. Chem. Rev. 114, 9708–9753 (2014).
- M. van Schilfgaarde, T. Kotani, S. Faleev, Quasiparticle self-consistent GW theory. Phys. Rev. Lett. 96,
- M. Oshikiri, M. Boero, J. Ye, F. Aryasetiawan, G. Kido, The electronic structures of the thin films of InVO₄ and TiO₂ by first principles calculations. Thin Solid Films 445, 168-174 (2003).
- H. Shang et al., Electron-phonon coupling in d-electron solids: A temperature-dependent study of rutile TiO₂ by first-principles theory and two-photon photoemission. Phys. Rev. Res. 1, 033153
- 61. U. Diebold, The surface science of titanium dioxide. Surf. Sci. Rep. 48, 53-229 (2003).
- K. Hashimoto, H. Irie, A. Fujishima, TiO₂ photocatalysis: A historical overview and future prospects. Jpn. J. Appl. Phys. 44, 8269 (2005).
- S. Wendt et al., The role of interstitial sites in the Ti_{3d} defect state in the band gap of titania. Science 320, 1755-1759 (2008).
- S. Moser et al., Tunable polaronic conduction in anatase TiO2. Phys. Rev. Lett. 110, 196403 (2013).
- J. Liu, X. Zhang, G. Lu, Excitonic effect drives ultrafast dynamics in van der Waals heterostructures. Nano Lett. 20, 4631-4637 (2020).
- A. L. Linsebigler, G. Lu, J. T. Yates Jr., Photocatalysis on TiO₂ surfaces: Principles, mechanisms, and selected results. Chem. Rev. 95, 735-758 (1995).
- A. Mills, S. Le Hunte, An overview of semiconductor photocatalysis. J. Photochem. Photobiol. A Chem. 108, 1-35 (1997).
- S. Zhou et al., Pseudospin-selective Floquet band engineering in black phosphorus. Nature 614, 75-80 (2023).
- Y. Dai et al., Poincaré engineering of surface plasmon polaritons. Nat. Rev. Phys. 4, 562–564 (2022). C. Di Valentin, A. Selloni, Bulk and surface polarons in photoexcited anatase TiO₂. J. Phys. Chem. Lett.
- 2, 2223-2228 (2011).
- J. P. Perdew, K. Burke, M. Ernzerhof, Generalized gradient approximation made simple. Phys. Rev. Lett. 77, 3865-3868 (1996).
- G. Kresse, J. Hafner, Ab initio molecular dynamics for liquid metals. Phys. Rev. B 47, 558-561 (1993).
- G. Kresse, J. Furthmüller, Efficiency of ab-initio total energy calculations for metals and semiconductors using a plane-wave basis set. Comput. Mater. Sci 6, 15-50 (1996).
- G. Kresse, J. Furthmüller, Efficient iterative schemes for ab initio total-energy calculations using a plane-wave basis set. Phys. Rev. B 54, 11169-11186 (1996).
- D. Bohm, D. Pines, A collective description of electron interactions. I. Magnetic interactions. Phys. Rev. 82, 625-634 (1951).
- D. Bohm, D. Pines, A collective description of electron interactions: III. Coulomb interactions in a degenerate electron gas. *Phys. Rev.* **92**, 609–625 (1953).

 77. J. C. Tully, Molecular dynamics with electronic transitions. *J. Chem. Phys.* **93**, 1061–1071 (1990).

 78. A. V. Akimov, O. V. Prezhdo, The PYXAID program for non-adiabatic molecular dynamics in
- condensed matter systems. J. Chem. Theory Comput. 9, 4959-4972 (2013).
- W. Chu et al., Ultrafast dynamics of photongenerated holes at a CH_3OH/TiO_2 rutile interface. J. Am. Chem. Soc. **138**, 13740–13749 (2016).
- X. Jiang, paraHFNAMD. Github. https://github.com/realxiangjiang/paraHFNAMD. Deposited 3 August 2023.
- A. Wang, Datasets-of-Anatase-TiO2. Github. https://github.com/AoleiWang/Datasets-of-Anatase-TiO2. Deposited 5 August 2023.